

UC Irvine

UC Irvine Previously Published Works

Title

Effect of Desiccating Stress on Mouse Meibomian Gland Function

Permalink

<https://escholarship.org/uc/item/98g2p15n>

Journal

The Ocular Surface, 12(1)

ISSN

1542-0124

Authors

Suhalim, Jeffrey L
Parfitt, Geraint J
Xie, Yilu
[et al.](#)

Publication Date

2014

DOI

10.1016/j.jtos.2013.08.002

Peer reviewed

Published in final edited form as:

Ocul Surf. 2014 January ; 12(1): 59–68. doi:10.1016/j.jtos.2013.08.002.

Effect of Desiccating Stress on Mouse Meibomian Gland Function

Jeffrey L. Suhalmi, PhD^{1,2,3}, Geraint J. Parfitt, PhD¹, Yilu Xie¹, Cintia S. De Pavia, MD⁴, Stephen C. Pflugfelder, MD⁴, Tejas N. Shah¹, Eric O. Potma, PhD², Donald J. Brown, PhD¹, and James V. Jester, PhD^{1,3}

¹Gavin Herbert Eye Institute, University of California, Irvine, CA

²Beckman Laser Institute and Medical Clinic, University of California, Irvine, CA

³Department of Biomedical Engineering, University of California, Irvine, CA

⁴Ocular Surface Center, Department of Ophthalmology, Baylor College of Medicine, Houston, TX, USA

Abstract

Purpose—Mice exposed to standardized desiccating environmental stress to induce dry eye-like symptoms have been used as a model to study the underlying mechanisms of evaporative dry eye. While studies have shown marked inflammatory and immune changes, the effect of such stress on meibomian gland function remains largely unknown. We sought to evaluate the effects of desiccating stress on meibocyte proliferation and meibum quality.

Methods—Ten mice were treated with scopolamine and subjected to a drafty low humidity environment (30–35%). Five and ten days after treatment, eyelids were harvested and cryosections stained with Ki67 antibody to identify cycling cells. Sections were also imaged using stimulated Raman scattering (SRS) microscopy to characterize the gland compositional changes by detecting the vibrational signatures of methylene (lipid) and amide-I (protein).

Results—Desiccating stress caused a 3-fold increase in basal acinar cell proliferation from 18.3 ± 11.1% in untreated mice to 64.4 ± 19.9% and 66.6 ± 13.4% after 5 and 10 days exposure, respectively ($P < .001$). In addition, SRS analysis showed a wider variation in the protein-to-lipid ratio throughout the gland, suggesting alterations in meibocyte differentiation and lipid synthesis.

Conclusions—These data are consistent with a model that a desiccating environment may have a direct effect on meibomian gland function, leading to a significant increase in basal acinar cell proliferation, abnormal meibocyte differentiation, and altered lipid production.

Keywords

evaporative dry eye; meibomian gland; nonlinear optical microscopy; stimulated Raman scattering

© 2013 Elsevier Inc. All rights reserved.

Single-copy reprint requests to James V. Jester, PhD. Corresponding author: James V. Jester, PhD, 843 Health Sciences Road, University of California, Irvine, Irvine, California, 92697-4390. TEL 949-824-8047. FAX 949-824-99626 JJester@uci.edu.

Publisher's Disclaimer: This is a PDF file of an unedited manuscript that has been accepted for publication. As a service to our customers we are providing this early version of the manuscript. The manuscript will undergo copyediting, typesetting, and review of the resulting proof before it is published in its final citable form. Please note that during the production process errors may be discovered which could affect the content, and all legal disclaimers that apply to the journal pertain.

The authors have no commercial or proprietary interest in any concept or product discussed in this article.

INTRODUCTION

Meibomian gland dysfunction (**MGD**) is the leading cause of dry eye disease,¹ which affects an estimated 21 million people in the United States alone.² Chronic dry eye, when left untreated, can lead to ophthalmic complications such as impaired vision and increased vulnerability to eye infections.³ Consequently, a better understanding of the progression of MGD may facilitate the development of effective therapeutic strategies against dry eye disease. In particular, comparative analysis of structural and biochemical features in normal and dysfunctional glands may reveal important insights into the pathophysiology of MGD.

Based on studies of dry eye patients and animal models, it has been noted that dry eye symptoms are accompanied by changes in meibomian gland structure, as well as in quality and quantity of glandular lipid secretion.^{4,5} In particular, alteration in meibum quality is likely to be a significant marker for MGD progression.⁶ In this regard, while structural abnormality such as terminal gland obstruction can be detected from excised eyelid by using H&E staining and standard optical microscopy,^{4,7,8} analyses of meibum have been primarily conducted using samples that are secreted or extracted from the gland.^{9–11} Without information pertaining to the gland structure, the mechanism that underpins meibum modification within dysfunctional glands cannot be directly observed. For example, it is unclear whether changes in meibum quality and quantity are a consequence of defective meibocytes, plugging of the duct, or other unknown phenomena.^{4,12} It has been suggested that meibum viscosity in MGD may increase due to the accumulation of protein,¹³ such as from cellular materials being sloughed off from the thickened epithelium.⁴ To further our understanding of MGD and dry eye disease, analysis of meibum content in the context of the glandular structure is essential.

Although characterizing meibum within the gland is important, it remains a challenging task. Common staining protocols such as H&E are generally unsuitable to study lipid-rich meibum, which readily dissolves in alcohol-based solvent.^{4,14} To our knowledge, there is no standardized protocol to assess the chemical makeup of meibum at different functional parts of the gland. A tool that is able to visualize and quantify lipid as well as protein-rich cellular materials in meibum within intact gland can potentially provide important clues to the mechanism that renders meibomian glands dysfunctional. Ideally, such a tool should also permit the application of other analytical methods such as immunohistochemistry and commonly used optical microscopy.

In recent years, stimulated Raman scattering (**SRS**) microscopy has been gaining popularity for label-free imaging of biological systems.^{15–17} Similar to second-harmonic generation (**SHG**) microscopy, SRS is a nonlinear optical technique in which the signal is not dependent on exogenous labels and does not require destructive sample preparation. SRS signals are derived from the molecular vibrations in the focal spot. By tuning the frequency of the excitation beams, different vibrational modes can be probed, enabling selective visualization of tissue components of interest. For example, the utility of SRS to detect carbon-hydrogen vibrations of lipid and cholesterol has been established for studies of fixed specimen, as well as live animals.^{18–20} Protein-rich materials can also be visualized by vibrationally tuning into protein-specific chemical groups such as the amide moiety.

In MGD, several studies have identified changes in relative quantities of protein-to-lipid (**P/L**) within expressed meibum and hypothesized the importance of having a specific P/L ratio.^{4,21–23} In the current study, we used the chemical group selectivity of SRS microscopy to quantify P/L ratios within the meibomian gland. Specifically, we combined immunofluorescence and label-free SRS microscopy to identify changes in meibomian glands of a dry eye mouse model. The dry eye mouse model has been recently developed

using desiccating stress consisting of low humidity (30–35%), continuous airflow, and inhibition of tear secretion by systemic scopolamine administration.^{24,25} Affected mice show ocular surface features that mimic evaporative dry eye in human; however, the response of the meibomian gland to such environmental stress has not been previously evaluated.

In this study, we monitored Ki-67 antigen staining to assess meibocyte proliferation and characterized meibum composition in different parts of the gland using SRS. We report for the first time that desiccating stress induced meibocyte cell cycle entry, suggesting abnormally high meibocyte proliferation and downstream meibum production in response to ocular surface desiccation. Furthermore, we show for the first time that while the protein content of normal meibum progressively decreases from the acini to orifice, suggesting meibum maturation, desiccating stress blocks maturation and leads to increased protein content within the meibum lipid. Based on these findings we propose that desiccating stress may induce meibomian gland dysfunction through altered meibocyte differentiation leading to changes in meibum quality.

II. MATERIALS AND METHODS

A. Mouse Model and Tissue Preparation

A total of ten adult female mice, 8 weeks old, (C57BL/6) were subjected to standardized desiccating stress conditions at the Ocular Surface Center, Baylor College of Medicine, as previously described.^{26,27} Mice were sacrificed after 5 and 10 days (n=5 and n=5, respectively). Untreated adult mice (n=5) were utilized for the control group. Exenterated eyes with intact eyelids were collected, embedded in OCT, cryosectioned (10 μ m thick sections) and placed on standard microscope slides. Slides were then shipped on dry ice to the Gavin Herbert Eye Institute for immunofluorescence and stimulated Raman scattering microscopy. Animal experiments were performed in accordance with the Institutional Animal Care and Use Committee protocol at Baylor College of Medicine and adhered to the ARVO Resolution on the Use of Animals in Vision Research.

B. Immunofluorescence Microscopy

Sections were air dried for 20 min, rehydrated in PBS (3 \times 5 min) and blocked with 10% goat serum at 37°C for 30 min. Anti-Ki67 (Abcam; 1mg/mL, 1/500 dilution) was applied to the tissue sections for overnight at 4°C. Sections were then washed in PBS (3 \times 5 min) and secondary antibody (Goat Anti-Rabbit AlexaFluor546; 1/1000 dilution) was applied to the sections for 1 hour at 37°C. Subsequently, sections were rinsed with PBS (3 \times 5 min), counterstained with DAPI (1:5000) and then mounted with a coverslip. Fluorescent imaging was performed on a Leica DMI6000B using a 20 \times /0.75NA objective. Digital images from both the upper and lower lid were taken from all 15 mouse eyes, and the numbers of Ki67 stained basal meibomian gland acinar cells counted as previously reported.²⁸

C. Stimulated Raman Scattering (SRS) Microscopy

A custom SRS microscope was utilized in this study.²⁰ The two laser beams required to generate stimulated Raman signals – known as the pump and Stokes beams-- were derived from an optical parametric oscillator (OPO, Levante Emerald, Berlin, Germany) pumped by a 7-ps, 76-MHz mode-locked Nd:YVO₄ laser (Picotrain, High-Q, Hohenems, Austria). The Stokes beam, at frequency ω_s , was provided by the Nd:YVO₄ laser and fixed at \sim 9,400 cm^{-1} throughout the experiments. The frequency of the pump beam, ω_p , was tuned in order to probe different molecular vibrational modes, $\omega_{\text{vib}} = |\omega_p - \omega_s|$. For example, the CH₂ bending and amide-I modes were probed by tuning the frequency differences, ω_{vib} , to 1440 and 1650 cm^{-1} , respectively.

The pump and Stokes beams were overlapped spatially and temporally and delivered to the tissue specimen via a 20 \times , 0.75 NA objective lens (UPlanSApo, Olympus) mounted on an inverted microscope (IX71, Olympus). Raster scanning at a rate of \sim 1 second per 512 by 512 pixels frame was realized using a laser scanner (Fluoview 300, Olympus, Center Valley, PA). The Stokes beam was modulated at 10 MHz using an acoustic optical modulator (Crystal technology, LLC). The transmitted pump beam was detected by a photodiode (FDS1010, Thorlabs) and electronically demodulated by a custom lock-in amplifier. The average combined power of the Stokes and pump beams at the specimen was maintained under 50 mW in order to avoid photodamage. The total time for generating an image with contrast based on the P/L ratio, including wavelength tuning and image averaging, was between 4 to 5 minutes for each region of interest (**ROI**). The relative standard error of ratiometric analysis of two different chemical modes is \sim 7%. No exogenous labels or stains were used for SRS, permitting direct use of the tissue sections for subsequent immunofluorescence imaging as described above. As a reference, Raman spectra from mouse meibomian gland were acquired using a commercial Raman microscope (InVia Confocal; Renishaw, Wotton-under-Edge, Gloucestershire, UK).

D. Protein-to-Lipid Ratio Analysis

The relative P/L ratio was obtained by tuning the SRS microscope to probe the presence of protein and lipid in the tissue specimen. Specifically, the signals at 1440 and 1650 cm^{-1} were utilized to measure the signal contribution from the CH_2 bending and amide-I modes, respectively.²⁹ Shown in Figure 1A is a Raman spectrum acquired from meibomian gland using a commercial Raman microscope. The two strongest peaks correspond to the CH_2 bending and amide-I modes. SRS images at the CH_2 bending and amide-I modes were generated using the custom SRS microscope and are shown in Figures 1B and C, respectively. After image acquisition at the two vibrational modes, a homogeneous background (baseline) was removed from each image by simple subtraction. To calculate P/L, pixel intensities from the amide-I image (**I₁₆₅₀**) were divided by the corresponding pixels from the CH_2 bending mode image (**I₁₄₄₀**). We experimentally verified that, in the lipophilic domains of the gland, the contributions from the OH-bending mode and the C=C stretching mode near the 1650 cm^{-1} vibrational energy are negligible relative to contribution of the amide-I mode. Given the unique presence of the amide-I mode in protein and the abundance of CH_2 groups in lipid molecules, the variation in **I₁₆₅₀ / I₁₄₄₀** correlates with the change of protein and lipid quantities in the sample. We note that the P/L ratio reported in this study is a relative quantity that does not represent the absolute mass ratio of protein and lipid.

III. RESULTS

A. SRS Imaging of Lipid in the Normal Mouse Meibomian Gland

The meibomian gland, which is comprised of lipid-producing meibocytes and secreted meibum lipid, can be visualized without exogenous labels via SRS microscopy. In Figure 2A, an SRS image of meibomian gland from normal adult mouse is shown. The image was acquired by tuning the laser beams to probe the CH_2 stretching vibrations at 2850 cm^{-1} ; therefore, bright pixels in the image can be attributed to CH-rich molecules, such as meibum lipid and protein in the gland.

Different regions of the gland can be discriminated based on the morphology and relative signal intensities. The acini (**ac**) are characterized by areas of diffuse SRS signals and dark circular spots (Figure 2A). These dark circular spots (red arrows) are devoid of lipids and are identified as the nuclei of meibocytes. The bright SRS signals at 2850 cm^{-1} from the acinar regions of the gland originate from CH-rich lipids in the cytosolic space of the meibocytes and mark the meibum-filled bodies of the cell. The transition from acinus

toward the gland's ductule (**dt**) is marked by the disintegration of meibocytes (yellow asterisk) and the release of intracellular lipids in the lumen of the gland. It can be seen that meibum within these regions emit stronger SRS signals than in the acini. It is possible that the secreted lipids and cellular debris from meibocytes accumulate in the ductule and become highly concentrated over time. The higher concentration of accumulated CH-rich molecules would in turn produce stronger SRS signals. Furthermore, the shape defined by the SRS signal resembles that of the ductule and the central duct as observed in H&E stained images of the meibomian gland.⁴

To corroborate these observations, the same tissue section was stained and imaged using a confocal fluorescence microscope. In Figure 2B, an overlay of the DAPI, Phalloidin, and SRS images (pseudo-colored respectively, red, blue and green) is shown. Signals from nuclei-specific DAPI filled up the dark circular holes in the SRS image, confirming that these lipidless areas correspond to cell nuclei. Consistent with observations from previous studies,^{28,30} there is virtually no DAPI signal in the center of the ductule and central duct regions where SRS signals are most intense, indicating a loss of cellular features in regions away from the acini. The rest of the DAPI signals are ubiquitous near the edges of the ductule and central duct, and can be attributed to stratified epithelial cells that line the ducts of the gland. Overall, the SRS image combined with the stained images provides a direct visualization of meibum distribution in the acini, disintegration area, ductule and central duct that leads to the opening of the orifice.

Previously, we have shown compositional variation among different regions of normal mouse meibomian glands using spectral coherent anti-Stokes Raman scattering (**CARS**) microscopy.³¹ In particular, data from CARS imaging and Raman spectroscopy suggested changes in protein contribution as meibum progresses from acinus to central duct. In this study, meibum composition at different portions of the gland was further investigated using SRS microscopy, a tool with higher sensitivity than CARS.

An overlay of SRS, DAPI and Phalloidin images of meibomian gland from an untreated adult mouse is shown in Figure 3A. Different regions of interest (**ROI**) within the gland are highlighted. Areas with overlapping SRS and DAPI signals (ROIs 1 to 5) were identified as acini. Disintegration areas and ductules were characterized by the presence of DAPI and strong SRS signals (ROIs 6 to 8), whereas the regions devoid of nuclei, yet exhibiting intense SRS signals, were categorized as the central duct. Figure 3B shows the corresponding P/L from each ROI. The acinar regions have higher P/L than ductules, and the central duct has the lowest P/L. This finding demonstrates that, in a normal gland, P/L decreases as meibum matures and progresses from acinus to ductule and central duct, confirming the hypothesis from our previous work.³¹ As a control, P/L of the extracellular tissue matrix (ROI 10), a reference for a region with high protein density, was determined to exhibit higher P/L than the lipid-filled acinus or central duct. Note that the SRS images were acquired at the CH₂ stretch mode $\sim 2850\text{ cm}^{-1}$ and shown solely for its enhanced contrast of the lipid distribution in the gland. The intensity of these images does not necessarily correlate with the P/L analysis of amide-I and CH₂ bending modes.

B. Effects of Desiccating Stress on Meibomian Gland Function

1. Gland Proliferation and Ductal Dilatation—Through immunostaining of cryosections (Figure 4), we evaluated the effect of desiccating stress on meibomian gland structure and function and identified ductal dilation and increased cell cycling in acinar and ductal epithelium at both day 5 and 10. Using antibodies against the nuclear, cell cycle associated protein, Ki67, immunostaining of control mouse eyelids (n=5) showed a normal gland structure with a low Ki67 labeling index of $18.3 \pm 11.1\%$ of basal acinar cells, similar to the previously reported values.^{28,30} However, mice exposed to 5 and 10 days (n=5 each) of

desiccating stress showed a significant increase ($P < .005$) in basal cell acinar staining averaging $64.4 \pm 19.9\%$ and $66.6 \pm 13.4\%$, respectively. While there is no marked increase ($P = .829$) in meibocyte proliferation between 5 and 10 days of exposure to desiccating stress, meibomian glands from mice exposed to 10 days of desiccating stress showed extensive ductal dilation, suggestive of increased meibum production and potentially duct obstruction (Figure 4; 10 Day, asterisk). It is therefore apparent that meibocytes proliferate, and are likely to increase meibum synthesis, to a much greater extent in a desiccating environment.

In summary, increased cell proliferation and structural changes that are pertinent to MGD were observed in the mouse model of dry eye. The observations here highlight the effect of desiccating stress to features of the glands from cellular to tissue-level. To further evaluate the impact of desiccating stress on meibomian gland function and meibum composition, we utilized the capability of SRS microscopy to generate images with P/L contrast.

2. Changes in Protein-to-Lipid Ratio (P/L)—P/L of meibum in the dry eye model was investigated in order to evaluate the effects of a desiccating environment on meibum composition. A representative SRS image of meibomian gland from a mouse after 5 days of treatment is shown in Figure 5A. Different ROIs, corresponding to acinus, ductule, and central duct, are highlighted. The dispersed bright spots in the extracellular matrix can be attributed to the presence of absorptive melanin pigments in the eyelid of C57BL/6 mouse, and play no further role in our P/L analysis of meibum. In contrast to the P/L trend observed from normal meibomian glands (Figure 3B), the P/L ratios in the dry eye model did not decrease from acinus to the central duct, revealing potential compositional changes in response to the dry eye environment.

In Figure 6A, an SRS image from one mouse sample after 10 days of treatment is shown. Meibum in the dilated central duct, as well as remnants of lipids in the acini, can be directly visualized. Interestingly, the P/L in this sample was lower in the central duct distal to the orifice compared to the acini – a feature similar to the control group (Figure 6B). However, moving proximally toward the orifice of the gland, the P/L ratio showed a gradual increase. Such a P/L trend is uncharacteristic of the expected P/L of normal glands, underscoring the compositional changes after 10-day-long treatment of desiccating stress.

In another mouse sample from the 10-day group (Figure 7), P/L also showed a modest increase toward the end of the central duct, ie, ROI 7. Hence, it can be inferred that deviation of the P/L trend from normal gland is independent of gland morphology. As such, despite the absence of apparent ductal dilation, both abnormal meibocyte proliferation and P/L trends occur in mice treated with desiccating stress. In Figure 8, the P/L trends of different mice are shown. For each individual mouse, P/L ratios from specific portions of the gland, eg, the P/L of multiple acini, were averaged and plotted as a single data point. Only glands with identifiable acinus, ductule, and central duct were included for comparison. Clearly, the dry eye mouse models of 5 days and 10 days (Figure 8B and C) exhibit different P/L trends from the untreated, control group (Figure 8A). While the P/L in normal glands consistently decreases as meibum progresses from acinus to central duct, mice of the dry eye model do not display a consistent P/L trend. These cases reveal compositional changes within mouse meibomian glands as a function of desiccating stress treatment, underlining the potential utility of P/L as a marker for dry eye disease and MGD.

IV. DISCUSSION

Many studies have established the correlation between MGD and symptoms of dry eye disease.¹ Specifically, changes in the quality of meibum and glandular structure have been noted^{4,10,11}; yet the underlying processes that drive the modification of meibum during

MGD progression have not yet been characterized. This study was designed to determine if desiccating stress can affect meibomian gland function and assess what compositional changes may occur in the meibum.

First, using SRS we identified that the P/L varies throughout different regions of the meibomian gland. Specifically in normal glands, P/L decreased from the acinus toward central duct, correlating with the loss of cellular structures as meibocytes disintegrated and released intracellular lipid.⁴ Interestingly, P/L also differed among acini from the same gland. Such difference may be caused by varying levels of protein or lipid associated with possible acinar cycles. Nevertheless, progressive decreases in protein as meibum flows through the duct toward the orifice suggests a maturation of meibum where protein is progressively degraded and removed from the lipid. Such a process has been previously suggested based on SDS PAGE analysis of meibum, where keratin proteins characteristic of the meibomian gland appear to be absent.^{32,33} The importance of removing proteins from meibum lipids has recently been emphasized by the finding that keratin proteins are disruptive to meibum lipid films, which may be a cause for decreased tear break-up time.²¹

Second, we identified that desiccating stress induces basal acinar cells to enter the cell cycle, perhaps increasing the proliferative rate by 3–4-fold within 5 to 10 days after induction of dry eye. This finding suggests that meibomian glands can respond dynamically to environmental stress, increasing meibocyte proliferation rate and potentially increasing the amount of meibum delivered to the tear film. While the mechanism controlling the meibomian gland response to environmental stress is unknown, meibomian glands are richly innervated by parasympathetic, sympathetic, and sensory nerve fibers.⁴ This pattern of innervation has prompted others to suggest that meibomian glands may be under similar neurosensory regulation as the lacrimal gland, and that they form part of a joint-functional unit with lacrimal gland and ocular surface.³⁴ Alternative mechanisms may also include hormonal regulation, growth factors, or inflammatory cytokines.⁴ Given the general lack of knowledge regarding physiologic regulation of the meibomian gland, further studies focusing on the effects of environmental stress on meibomian gland may provide important insights into the specific mechanism(s) responsible for the glandular response. On this note, additional studies to verify the absence of direct effects of scopolamine on the meibomian gland, other than blocking lacrimal gland function, may corroborate its use for investigating the linkage between MGD and evaporative dry eye.

Since previous studies of meibocyte proliferation in normal mice indicate that meibocyte cycling is below 30%,^{28,30} dramatically increased cell proliferation may also have important downstream effects on gland function. In general, the production of lipid from meibomian glands is due to the proliferation and differentiation of basal acinar cells, which are thought to be continually replenished by a meibocyte stem cell pool.^{4,35} Continual or repeated exposure to desiccating stress may therefore potentially deplete meibocyte stem cells and lead to early aging changes and gland atrophy. Such a mechanism may explain recent findings of increased meibomian gland dysfunction in contact lens wearers,³⁶ as well as in video display terminal workers, who show decreased spontaneous blink patterns and increased incidence of meibomian gland dysfunction.^{37,38} To this end, studies on the effects of desiccating stress on meibomian gland stem cells may advance the understanding of the pathophysiologic mechanisms associated with these disorders.

Third, P/L in mice after 5 and 10 days of desiccating stress showed altered trends in comparison to the P/L trend in untreated mice. In some cases from both 5- and 10-day exposure, P/L ratios remained generally the same throughout different portions of the glands, whereas other cases showed decreased P/L from acinus to ductule but increased P/L toward the end of the central duct and/or orifice following 10 days exposure. These findings

suggest that the rate of meibum production induced by desiccating stress may exceed the ability to remove or degrade protein. Since keratins are the major proteins expressed by ductal and acinar epithelial cells, persistence of keratin proteins in the meibum lipids may lead to altered lipid quality and fluidity.²¹ This possibility is supported by the finding that many of the glands showed ductal dilation suggesting plugging of the gland. While plugging may have been due to hyperkeratinization of the gland orifice, the past finding that patients with meibomian gland dysfunction showed increased protein and keratin content^{10,23,33} suggest an alternative mechanism involving abnormal meibum lipid maturation and retention of keratin proteins. While these results need to be repeated, future studies on the mechanisms that control protein and perhaps DNA degradation within the meibomian gland duct may provide additional clues into the pathogenesis of meibomian gland dysfunction.

Importantly, this study demonstrated the utility of SRS in combination with fluorescent cytochemistry to characterize changes within the meibomian gland. Whereas cellular and structural changes of the gland can be visualized using standard optical and stain-based techniques, the spatial and compositional analysis of meibum quality within the gland requires an imaging tool with chemical selectivity. Samples prepared for H&E staining that have been treated with alcohol-based solvents dissolve the meibum lipids and preclude a meaningful chemical analysis of the gland. Lipophilic stains such as Oil Red O and Nile Red can be used to visualize the general distribution of lipids; however, the lack of accuracy and chemical specificity limit their application for reliable quantitative lipid analysis.^{39–41} In this regard, label-free SRS microscopy circumvents these complications. Biological components comprising different chemical functional groups exhibit distinguishable vibrational Raman signatures.

In 2009, Oshima et al utilized spontaneous Raman spectroscopy to obtain Raman signatures of secreted meibum from normal and dry eye patients.⁴² Chemical variation of meibum was observed, demonstrating the potential of Raman-based techniques for study of meibum processed from the glands. Nevertheless, several features of spontaneous Raman spectroscopy also hinder its usage for quantitative imaging of tissue.^{16,43} First, the weak spontaneous Raman signal translates into slow acquisition times that are impractical for imaging biological tissues over large areas. Second, autofluorescence can overwhelm the weak Raman signals, complicating subsequent quantification of the image. Autofluorescence signals can be mitigated by using excitation beams in the near-infrared region, albeit at the cost of signal generation efficiency and imaging speed. Coherent Raman scattering techniques are free from the aforementioned limitations and exhibit much faster image acquisition times, up to video-rate.^{16,17,44} In principle, Raman-based imaging does not require specific sample preparation, and thus the same tissue samples can be readily re-analyzed with other methods such as immunofluorescence as shown in this study.

In our previous study, we showed the utility of CARS microscopy to detect compositional variation at different parts of the glands.³¹ In this study, we utilized SRS microscopy to further characterize the variation in normals and a dry eye mouse model. SRS is free from the unwanted, nonresonant background present in CARS.¹⁷ The absence of the nonresonant background and the linear dependence on concentration favors the use of SRS for reliable quantitative ratiometric Raman analysis. Moreover, SRS enables chemical imaging in the congested fingerprint region in the 1000–1800 cm^{-1} range. Although the carbon-hydrogen stretching mode at $\sim 2945 \text{ cm}^{-1}$ is generally a good Raman indicator for structural proteins in tissue,⁴⁵ it is not exclusive to protein. In addition, many lipophilic compounds such as cholesterol and cholesteryl esters also have notable contributions in this vibrational range. In contrast, the amide-I peak in the fingerprint region at $\sim 1650 \text{ cm}^{-1}$ can be used as an exclusive marker for protein. For the P/L analysis, we chose to analyze the intensity ratio of amide-I and CH_2 bending modes because the peak locations are relatively close, $\sim 210 \text{ cm}^{-1}$

apart, which in practice minimizes the spectral tuning time of the pump beam and reduces the acquisition time. Although neither the CH₂ stretching modes nor the CH₂ bending modes are exclusive to lipid, the density of methylene groups in aliphatic lipids is so high that the methylene vibrational modes constitute a proven marker for lipids.

We plan to extend the study reported here to construct three-dimensional P/L map in order to gain a more comprehensive analysis of meibum quantity and quality at different portions of the gland. Based on our recent study of MGD using 3D immunofluorescent computed tomography, several features of the disease are mostly apparent when the whole glandular tissue is in view.^{30,46} The intrinsic optical sectioning capability of SRS facilitates such 3D reconstruction of chemical maps. We anticipate that P/L analysis of whole glandular tissue would unravel differences between normal and dry eye cases hitherto hidden from view. Additionally, two groups have also pointed out variation of cholesteryl and wax ester composition in meibum as a function of MGD progression and age.^{11,47} The sensitivity of SRS to detect the presence of various lipophilic compounds may also be useful to identify the location and origin of such changes within the gland.

Overall, the observations reported here offers unique insights into the response of the meibomian gland to desiccating stress and suggest novel mechanisms regarding meibomian gland function and dysfunction. Additionally, findings in this study demonstrate the application of SRS to identify meibum changes within the glandular structure, paving the way toward better understanding of the pathophysiology of MGD. Combined with immunofluorescence, the interplay between meibocyte proliferation, meibum composition, and structural changes of the gland, can be directly visualized. While the utility of P/L as a marker for MGD requires further investigation, it is clear that the addition of SRS analysis to future studies may be of great value.

Acknowledgments

Supported in part by NEI EY021510, Discovery Eye Foundation; the Skirball Program in Molecular Ophthalmology and Research to Prevent Blindness, Inc; National Institutes of Health grant P41-RR01192 (Laser Microbeam and Medical Program); and by the Beckman Foundation.

REFERENCES

1. Mathers WD, Lane JA. Meibomian gland lipids, evaporation, and tear film stability. *Adv Exp Med Biol.* 1998; 438:349–360. [PubMed: 9634908]
2. Dry eye: an update on clinical diagnosis, management and promising new treatments. St. Louis, MO: Market Scope; 2004.
3. Lemp MA. Epidemiology and classification of dry eye. *Adv Exp Med Biol.* 1998; 438:791–803. [PubMed: 9634969]
4. Knop E, Knop N, Millar T, et al. The international workshop on meibomian gland dysfunction: report of the subcommittee on anatomy, physiology, and pathophysiology of the meibomian gland. *Invest Ophthalmol Vis Sci.* 2011; 52:1938–1978. [PubMed: 21450915]
5. Nichols KK, Foulks GN, Bron AJ, et al. The international workshop on meibomian gland dysfunction: executive summary. *Invest Ophthalmol Vis Sci.* 2011; 52:1922–1929. [PubMed: 21450913]
6. Ashraf Z, Pasha U, Greenstone V, et al. Quantification of human sebum on skin and human meibum on the eye lid margin using Sebutape(R), spectroscopy and chemical analysis. *Curr Eye Res.* 2011; 36:553–562. [PubMed: 21591865]
7. Jester JV, Nicolaidis N, Smith RE. Meibomian gland studies: histologic and ultrastructural investigations. *Invest Ophthalmol Vis Sci.* 1981; 20:537–547. [PubMed: 7194327]

8. Matsumoto Y, Sato EA, Ibrahim OM, et al. The application of in vivo laser confocal microscopy to the diagnosis and evaluation of meibomian gland dysfunction. *Mol Vis.* 2008; 14:1263–1271. [PubMed: 18618006]
9. Butovich IA, Arciniega JC, Lu H, Molai M. Evaluation and quantitation of intact wax esters of human meibum by gas-liquid chromatography-ion trap mass spectrometry. *Invest Ophthalmol Vis Sci.* 2012; 53:3766–3781. [PubMed: 22531701]
10. Borchman D, Foulks GN, Yappert MC, Milliner SE. Differences in human meibum lipid composition with meibomian gland dysfunction using NMR and principal component analysis. *Invest Ophthalmol Vis Sci.* 2012; 53:337–347. [PubMed: 22131391]
11. Joffre C, Souchier M, Gregoire S, et al. Differences in meibomian fatty acid composition in patients with meibomian gland dysfunction and aqueous-deficient dry eye. *Br J Ophthalmol.* 2008; 92:116–119. [PubMed: 18156378]
12. Tomlinson A, Bron AJ, Korb DR, et al. The international workshop on meibomian gland dysfunction: report of the diagnosis subcommittee. *Invest Ophthalmol Vis Sci.* 2011; 52:2006–2049. [PubMed: 21450918]
13. Borchman D, Foulks GN, Yappert MC, et al. Human meibum lipid conformation and thermodynamic changes with meibomian-gland dysfunction. *Invest Ophthalmol Vis Sci.* 2011; 52:3805–3817. [PubMed: 21398284]
14. Fukumoto S, Fujimoto T. Deformation of lipid droplets in fixed samples. *Histochem Cell Biol.* 2002; 118:423–428. [PubMed: 12432454]
15. Potma EO, Cheng JX, Xie XS. Coherent Raman imaging techniques and biomedical applications. *J Biomed Opt.* 2011; 16:021101. [PubMed: 21361664]
16. Min W, Freudiger CW, Lu S, Xie XS. Coherent nonlinear optical imaging: beyond fluorescence microscopy. *Annu Rev Phys Chem.* 2011; 62:507–530. [PubMed: 21453061]
17. Cheng, J-X.; Xie, XS. Coherent Raman scattering microscopy. Boca Raton: CRC Press; 2013.
18. Shi Y, Zhang D, Huff TB, et al. Longitudinal in vivo coherent anti-Stokes Raman scattering imaging of demyelination and remyelination in injured spinal cord. *J Biomed Opt.* 2011; 16:106012. [PubMed: 22029359]
19. Belanger E, Henry FP, Vallee R, et al. In vivo evaluation of demyelination and remyelination in a nerve crush injury model. *Biomed Opt Express.* 2011; 2:2698–2708. [PubMed: 22091449]
20. Suhaim JL, Chung CY, Lilledahl MB, et al. Characterization of cholesterol crystals in atherosclerotic plaques using stimulated Raman scattering and second-harmonic generation microscopy. *Biophys J.* 2012; 102:1988–1995. [PubMed: 22768956]
21. Palaniappan CK, Schutt BS, Brauer L, et al. Effects of keratin and lung surfactant proteins on the surface activity of meibomian lipids. *Invest Ophthalmol Vis Sci.* 2013; 54:2571–2581. [PubMed: 23482461]
22. Green-Church KB, Butovich I, Willcox M, et al. The international workshop on meibomian gland dysfunction: report of the subcommittee on tear film lipids and lipid-protein interactions in health and disease. *Invest Ophthalmol Vis Sci.* 2011; 52:1979–1993. [PubMed: 21450916]
23. Borchman D, Yappert MC, Foulks GN. Changes in human meibum lipid with meibomian gland dysfunction using principal component analysis. *Exp Eye Res.* 2010; 91:246–256. [PubMed: 20546726]
24. Stern ME, Beuerman RW, Fox RI, et al. The pathology of dry eye: the interaction between the ocular surface and lacrimal glands. *Cornea.* 1998; 17:584–589. [PubMed: 9820935]
25. Stern ME, Beuerman RW, Fox RI, et al. A unified theory of the role of the ocular surface in dry eye. *Adv Exp Med Biol.* 1998; 438:643–651. [PubMed: 9634949]
26. De Paiva CS, Chotikavanich S, Pangelinan SB, et al. IL-17 disrupts corneal barrier following desiccating stress. *Mucosal Immunol.* 2009; 2:243–253. [PubMed: 19242409]
27. Dursun D, Wang M, Monroy D, et al. A mouse model of keratoconjunctivitis sicca. *Invest Ophthalmol Vis Sci.* 2002; 43:632–638. [PubMed: 11867577]
28. Nien CJ, Paugh JR, Massei S, et al. Age-related changes in the meibomian gland. *Exp Eye Res.* 2009; 89:1021–1027. [PubMed: 19733559]
29. De Gelder J, De Gussem K, Vandenabeele P, Moens L. Reference database of Raman spectra of biological molecules. *J Raman Spectrosc.* 2007; 38:1133–1147.

30. Parfitt GJ, Xie Y, Reid KM, et al. A novel immunofluorescent computed tomography (ICT) method to localise and quantify multiple antigens in large tissue volumes at high resolution. *PLoS One*. 2012; 7:e53245. [PubMed: 23300899]
31. Lin CY, Suhaim JL, Nien CL, et al. Picosecond spectral coherent anti-Stokes Raman scattering imaging with principal component analysis of meibomian glands. *J Biomed Opt*. 2011; 16:021104. [PubMed: 21361667]
32. Jester JV, Nicolaidis N, Smith RE. Meibomian gland dysfunction. I. Keratin protein expression in normal human and rabbit meibomian glands. *Invest Ophthalmol Vis Sci*. 1989; 30:927–935. [PubMed: 2470693]
33. Ong BL, Hodson SA, Wigham T, et al. Evidence for keratin proteins in normal and abnormal human meibomian fluids. *Curr Eye Res*. 1991; 10:1113–1119. [PubMed: 1724955]
34. Knop, N.; Knop, E. *Ophthalmologie*. Vol. 106. German: 2009. Meibomian glands. Part I: anatomy, embryology and histology of the meibomian glands; p. 872-883.
35. Olami Y, Zajicek G, Cogan M, et al. Turnover and migration of meibomian gland cells in rats' eyelids. *Ophthalmic Res*. 2001; 33:170–175. [PubMed: 11340409]
36. Arita R, Itoh K, Inoue K, et al. Contact lens wear is associated with decrease of meibomian glands. *Ophthalmology*. 2009; 116:379–384. [PubMed: 19167077]
37. Freudenthaler N, Neuf H, Kadner G, Schlote T. Characteristics of spontaneous eyeblink activity during video display terminal use in healthy volunteers. *Graefes Arch Clin Exp Ophthalmol*. 2003; 241:914–920. [PubMed: 14586592]
38. Fenga C, Aragona P, Cacciola A, et al. Meibomian gland dysfunction and ocular discomfort in video display terminal workers. *Eye*. 2008; 22:91–95. [PubMed: 17962818]
39. Wang MC, Min W, Freudiger CW, et al. RNAi screening for fat regulatory genes with SRS microscopy. *Nat Methods*. 2011; 8:135–138. [PubMed: 21240281]
40. Hellerer T, Axang C, Brackmann C, et al. Monitoring of lipid storage in *Caenorhabditis elegans* using coherent anti-Stokes Raman scattering (CARS) microscopy. *Proc Natl Acad Sci U S A*. 2007; 104:14658–14663. [PubMed: 17804796]
41. Kinkel AD, Fernyhough ME, Helterline DL, et al. Oil red-O stains non-adipogenic cells: a precautionary note. *Cytotechnology*. 2004; 46:49–56. [PubMed: 19003258]
42. Oshima Y, Sato H, Zaghoul A, et al. Characterization of human meibum lipid using raman spectroscopy. *Curr Eye Res*. 2009; 34:824–835. [PubMed: 19895310]
43. Suhaim JL, Boik JC, Tromberg BJ, Potma EO. The need for speed. *J Biophotonics*. 2012; 5:387–395. [PubMed: 22344721]
44. Saar BG, Freudiger CW, Reichman J, et al. Video-rate molecular imaging in vivo with stimulated Raman scattering. *Science*. 2010; 330:1368–1370. [PubMed: 21127249]
45. Lu FK, Ji M, Fu D, et al. Multicolor stimulated Raman scattering (SRS) microscopy. *Mol Phys*. 2012; 110:1927–1932. [PubMed: 23504195]
46. Jester BE, Nien CJ, Winkler M, et al. Volumetric reconstruction of the mouse meibomian gland using high-resolution nonlinear optical imaging. *Anat Rec (Hoboken)*. 2011; 294:185–192. [PubMed: 21234992]
47. Borchman D, Foulks GN, Yappert MC, Milliner SE. Changes in human meibum lipid composition with age using nuclear magnetic resonance spectroscopy. *Invest Ophthalmol Vis Sci*. 2012; 53:475–482. [PubMed: 22169100]

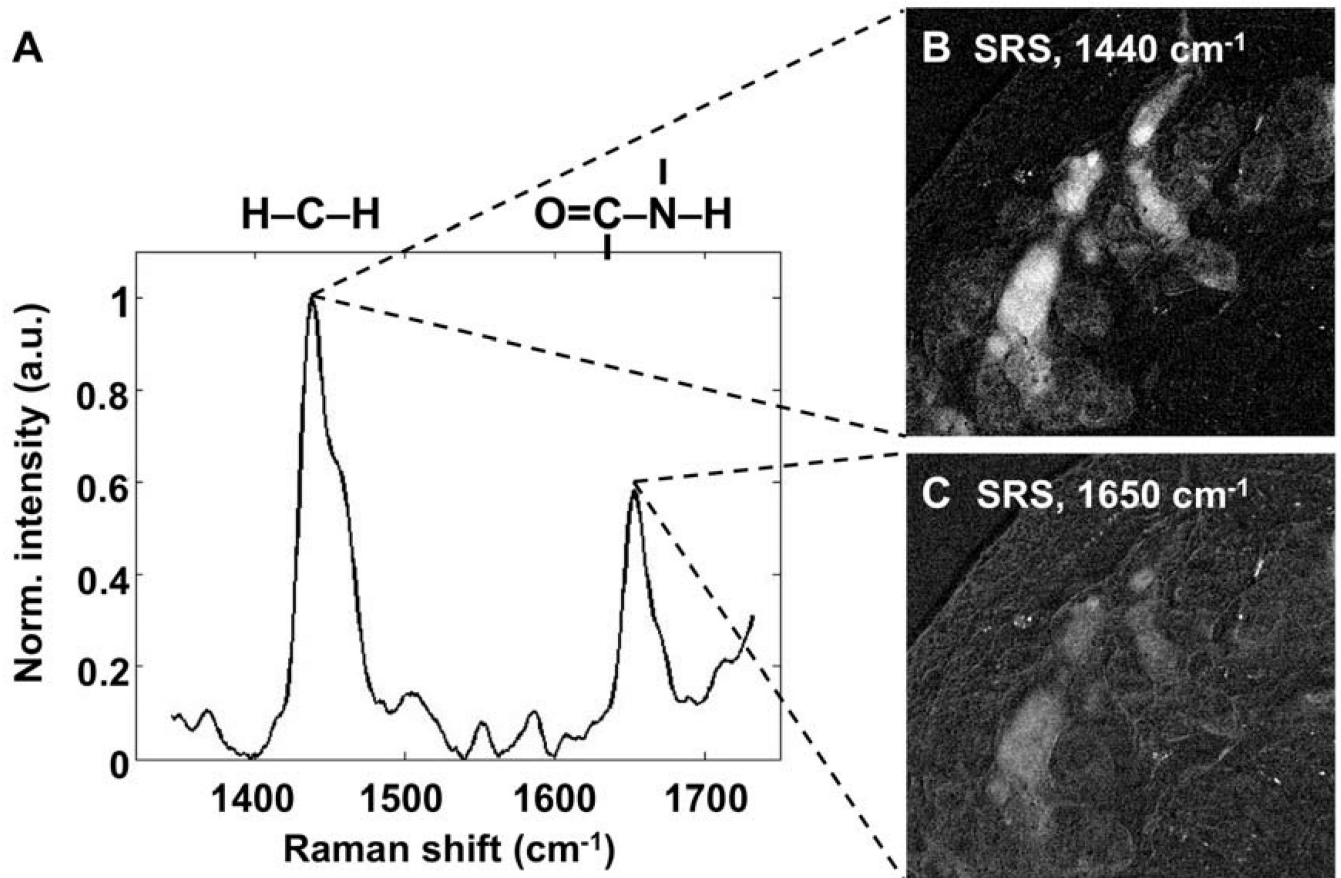


Figure 1.

A) Reference raman spectrum acquired from a single point in mouse meibomian gland. For SRS imaging, two laser beams at different optical frequencies were utilized to probe the vibrational resonance of the CH₂ bending (1440 cm⁻¹) and amide-I (1650 cm⁻¹) modes, representing the lipid and protein markers, respectively. Laser beams were scanned through the tissue section via an inverted microscope. Resulting images at 1440 cm⁻¹ and 1650 cm⁻¹ modes are shown in panel B and C, respectively. Protein-to-lipid ratios (P/L) were calculated by dividing the pixel intensities at 1650 cm⁻¹ with intensities at 1440 cm⁻¹. Image width in Panel B and C is 353.5 μm.

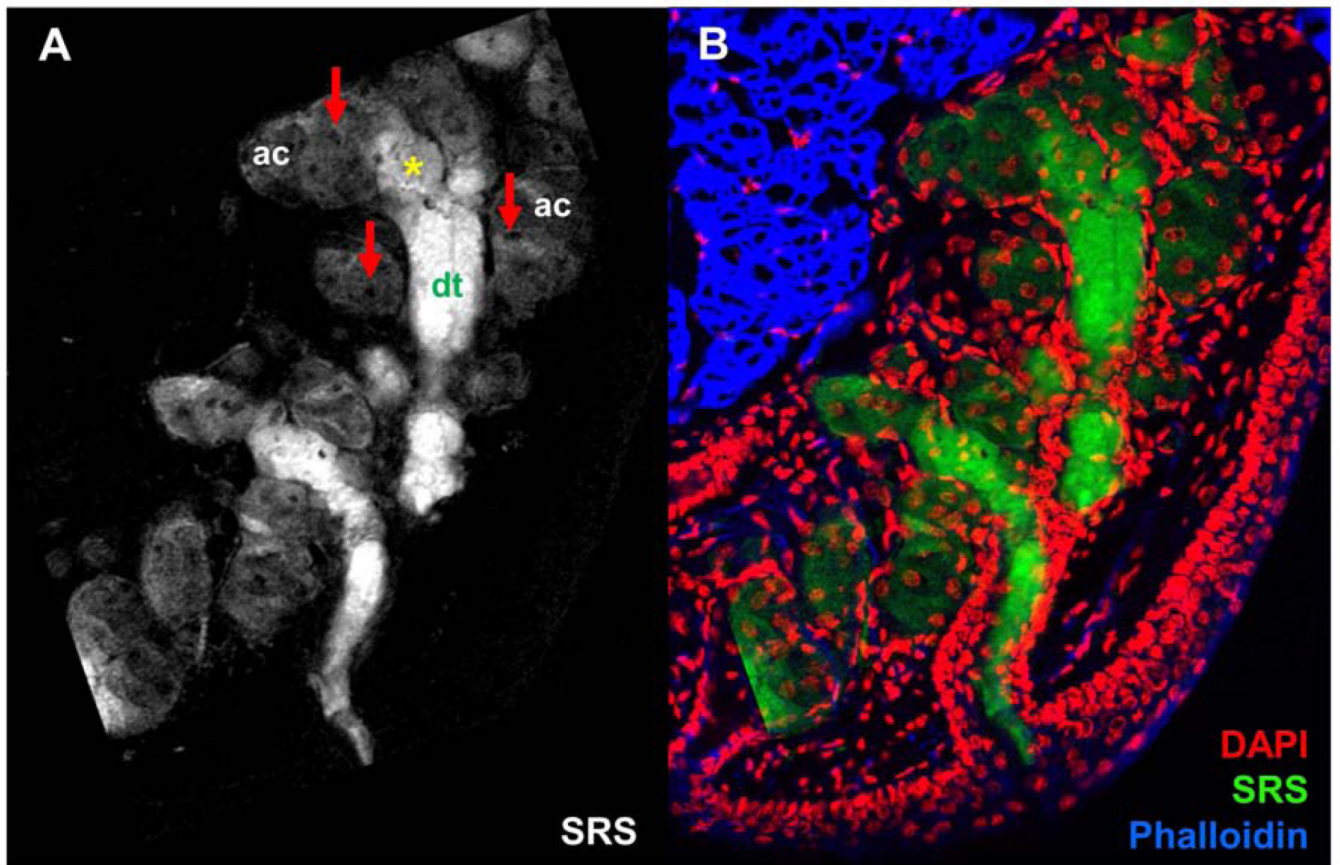


Figure 2.

A) Chemical-selective imaging meibomian gland excised from normal, untreated mouse using stimulated Raman scattering (SRS). SRS image was acquired at the CH₂ stretching mode. Red arrows point at cell nuclei. Asterisk marks disintegration area. ac, acini; dt, ductule. B) Overlay of DAPI (red), SRS (green), and Phalloidin (blue) images, highlighting the distribution of meibum, cell nuclei and actin in context of the glandular structure. Scale bar is 100 μ m.

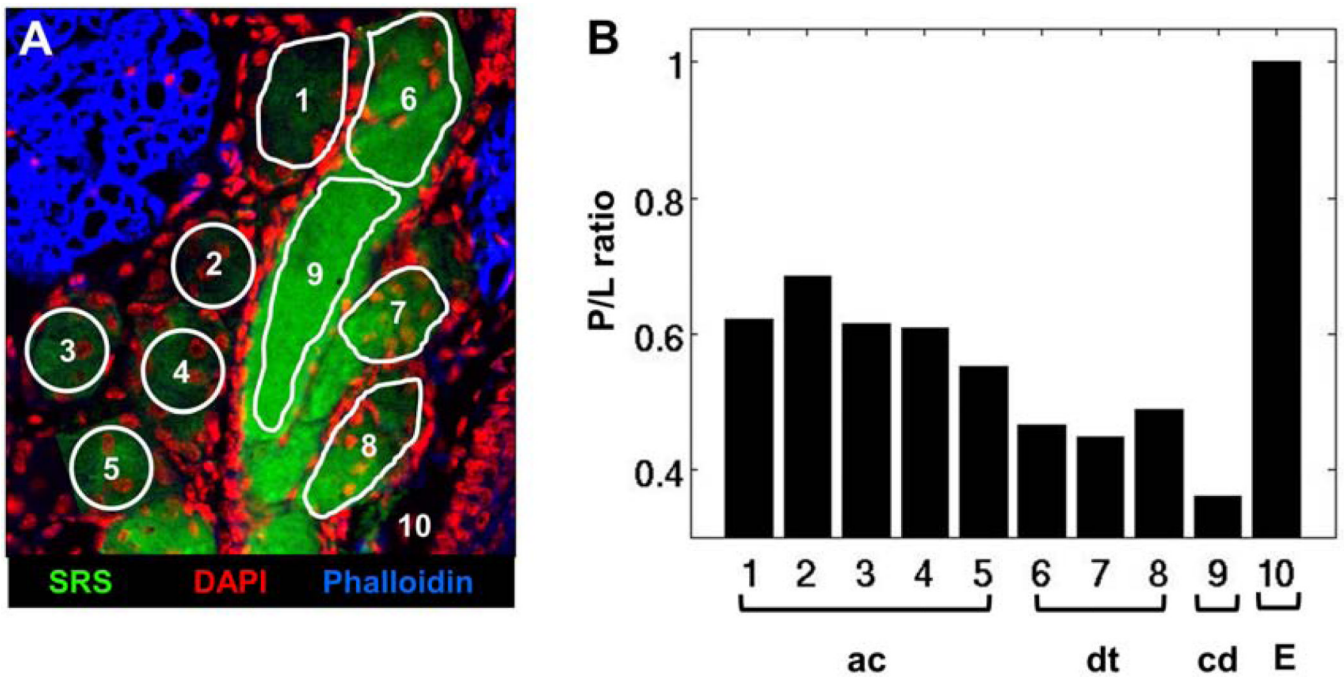


Figure 3.

P/L ratio in meibum of normal, untreated mouse gland. A) Overlay of SRS (green), DAPI (red) and Phalloidin (blue) images of meibomian gland from normal, untreated mouse. B) Protein-to-lipid ratio (P/L) from ROIs highlighted in panel A. The duct and central duct exhibit lower P/L than acini, correlating with the lower level of nuclei-specific DAPI staining. ac, acinus; dt, ductule; cd, central duct; E, extracellular matrix. Image width is 237 μm .

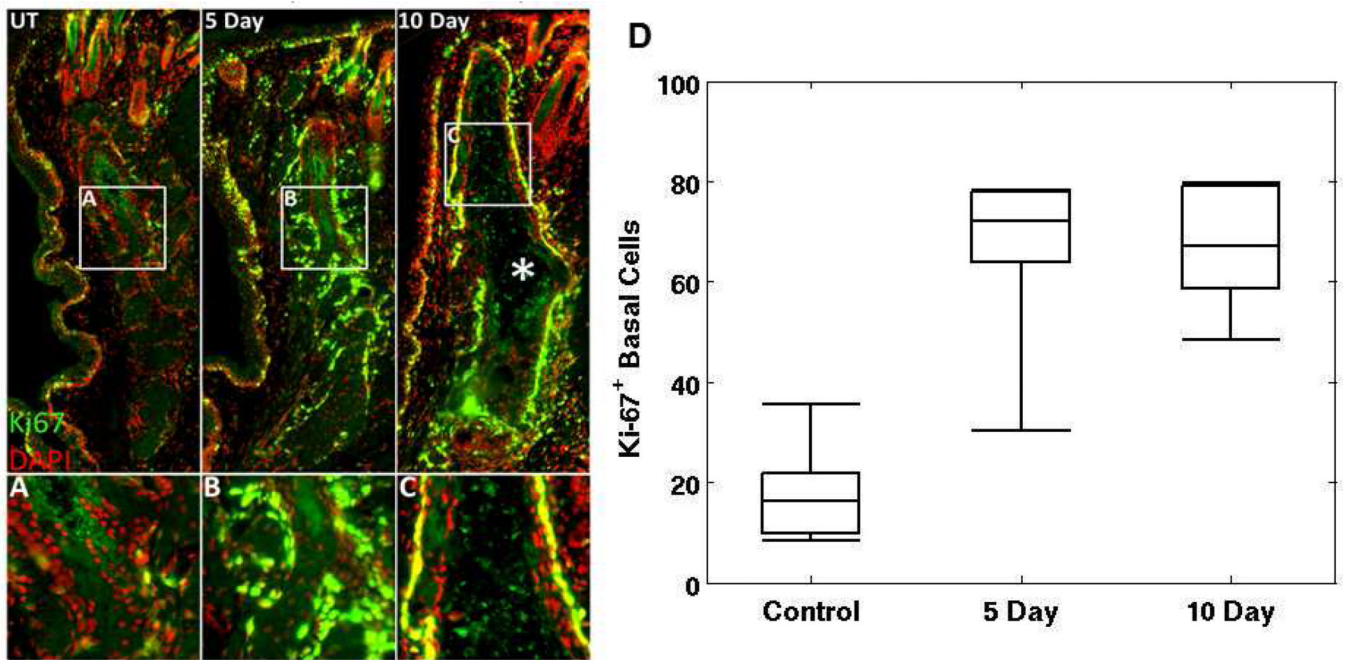


Figure 4.

Ductal dilation and increased Ki67 staining were observed in meibomian glands of dry eye mouse model. Shown in panel A is an overlay of Ki67 (green) and DAPI (red) stained images of meibomian gland from untreated, normal mice. Panel B and C show stained images of glands from mice treated in a desiccating stress environment for 5 and 10 days, respectively. In panel D, the average number of cells that show positive Ki-67⁺ stain under each categories are shown. Central line marks the median.

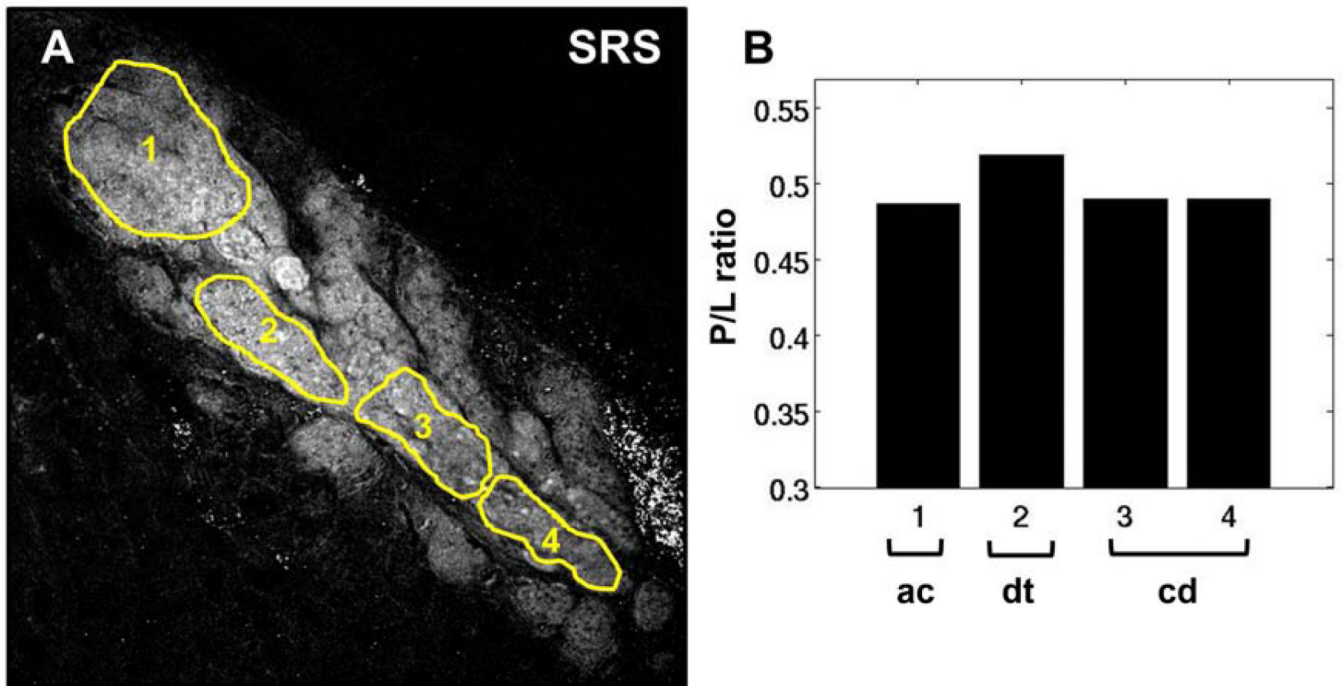


Figure 5. P/L ratio in meibum of mouse treated in a desiccating stress environment for 5 days. (A) SRS image acquired at the CH₂ stretching mode. (B) P/L ratio corresponding to the highlighted ROIs in panel A. The overall P/L trend here differs from the trend observed in the untreated, control mice. ac, acinus; dt, ductule; cd, central duct. Scale bar is 100 μ m.

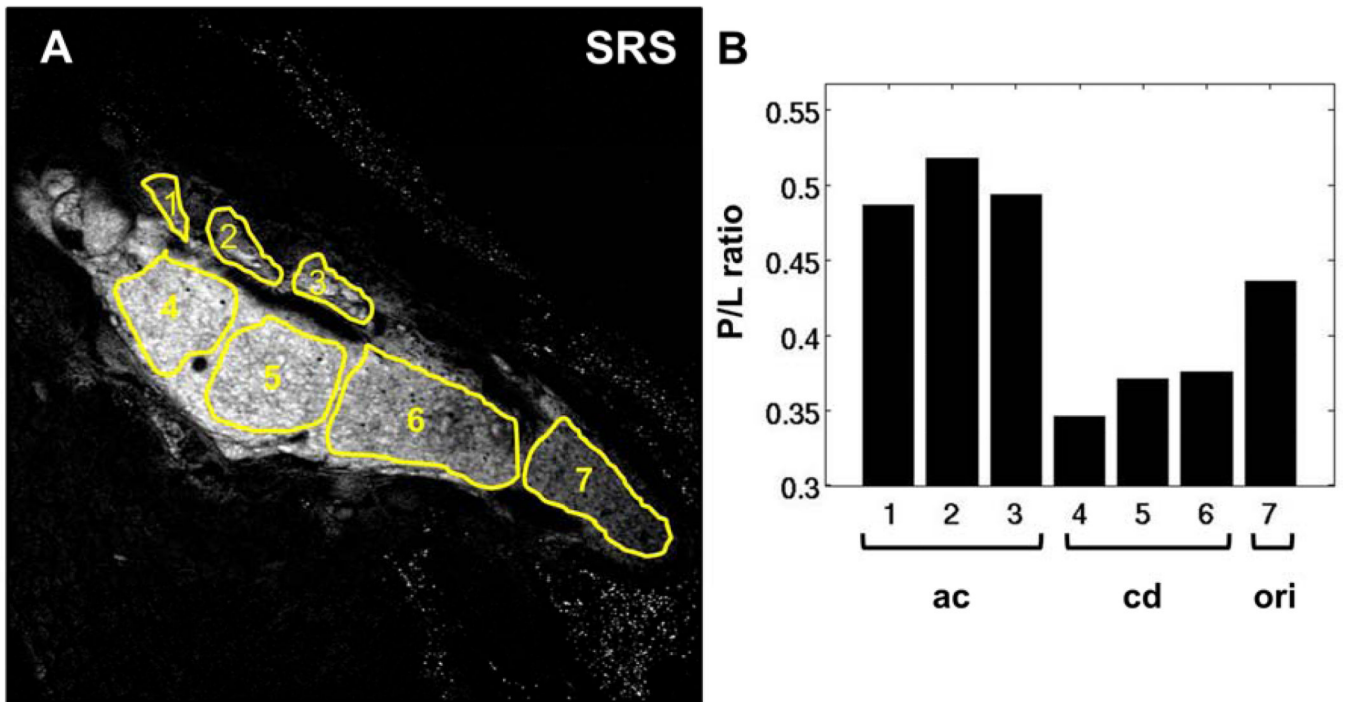


Figure 6. P/L ratio in meibum of mouse treated in a desiccating stress environment for 10 days. (A) SRS image acquired at the CH₂ stretching mode. (B) P/L ratio corresponding to the highlighted ROIs in panel A. P/L initially decreases from acini to central duct; however, moving proximally towards the orifice of the gland, P/L gradually increases. ac, acinus; dt, ductule; cd, central duct. Scale bar is 100 μ m.

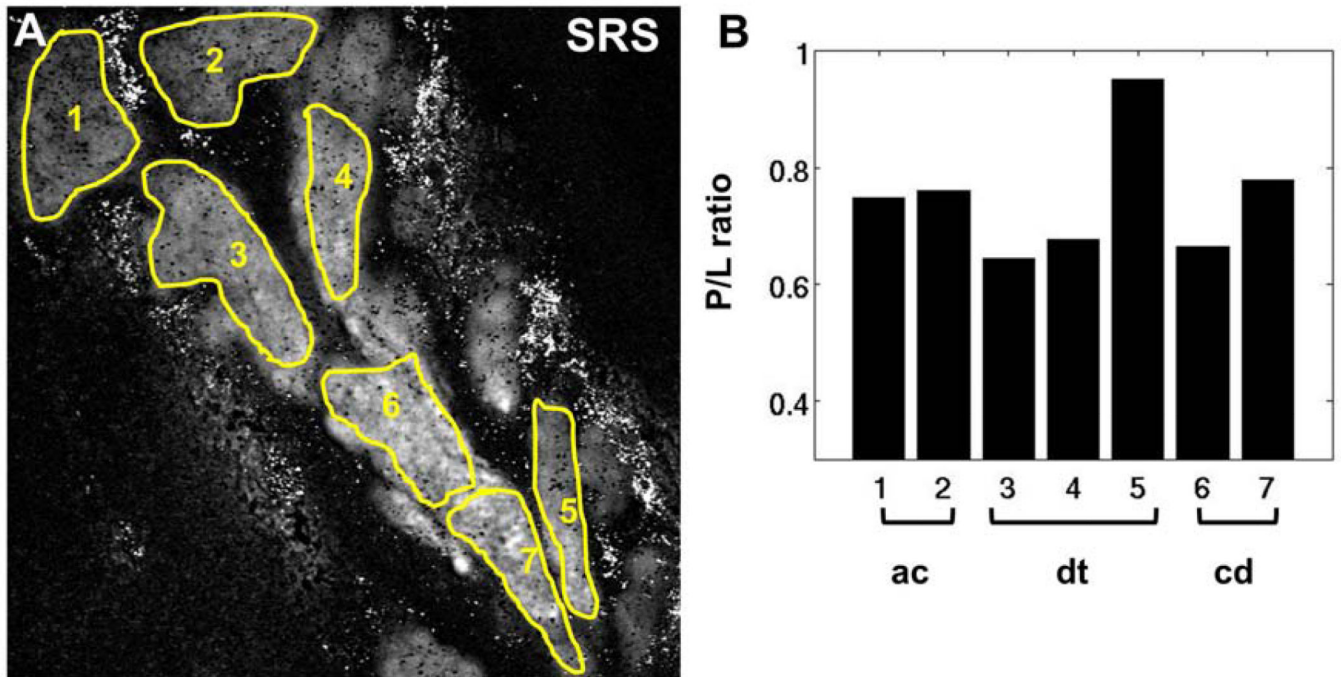


Figure 7. P/L ratio in meibum of mouse treated in a desiccating stress environment for 10 days. (A) SRS image at the CH₂ stretching mode. (B) P/L ratio corresponding to the highlighted ROIs in panel A. Despite the absence of ductal dilation as observed in Fig. 5, the overall P/L progression from acini to central duct nonetheless deviate from the trend observed in the untreated, control mice. ac, acinus; dt, ductule; cd, central duct. Scale bar is 50 μ m.

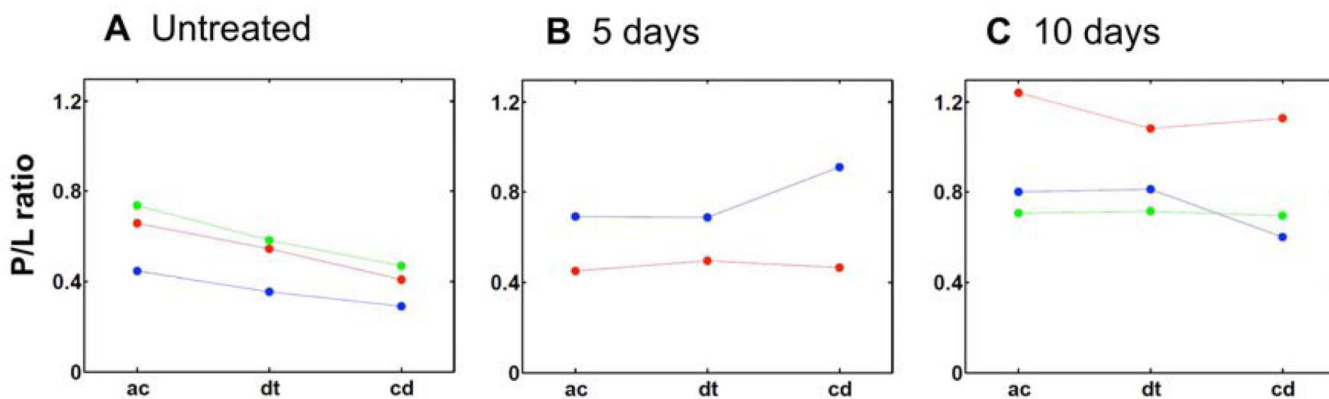


Figure 8.

Comparison between P/L ratios of untreated and dry eye mice. The average P/L ratios (filled circle) are plotted as a function of location in the meibomian gland, i.e., acini, ductule and central duct (including orifice). Different colors are used to represent measurement from different animals, whereas connecting line is drawn to highlight P/L changes from acini to central duct within the same animal. In panel A, it can be seen that P/L ratios of untreated mice consistently decrease from acinus (ac) to ductule (dt) to central duct (cd). On the other hand, P/L ratios of dry eye mice (panel B and C) do not follow the same trend as the untreated group (panel A), underlining changes in meibum quality in response to desiccating stress.